

Retrofitting an atomic force microscope with photothermal excitation for a clean cantilever response in low Q environments

Aleksander Labuda,¹ Kei Kobayashi,² Yoichi Miyahara,¹ and Peter Grütter¹

¹Department of Physics, McGill University, Montreal, Quebec H3A 2T8, Canada

²Office of Society-Academia Collaboration for Innovation, Kyoto University, Katsura, Nishikyo, Kyoto 615-8520, Japan

(Received 27 February 2012; accepted 22 April 2012; published online 10 May 2012)

It is well known that the low- Q regime in dynamic atomic force microscopy is afflicted by instrumental artifacts (known as “the forest of peaks”) caused by piezoacoustic excitation of the cantilever. In this article, we unveil additional issues associated with piezoacoustic excitation that become apparent and problematic at low Q values. We present the design of a photothermal excitation system that resolves these issues, and demonstrate its performance on force spectroscopy at the interface of gold and an ionic liquid with an overdamped cantilever ($Q < 0.5$). Finally, challenges in the interpretation of low- Q dynamic AFM measurements are discussed. © 2012 American Institute of Physics. [<http://dx.doi.org/10.1063/1.4712286>]

I. INTRODUCTION

Dynamic atomic force microscopy¹ (dAFM) has become a ubiquitous tool in surface science in the last two decades, and its versatility is made evident by the wide span of studies in environments ranging from ultrahigh vacuum, to cryogenic temperatures, and to liquids. It has recently been identified that piezoacoustic excitation of cantilevers can prevent accurate interpretation of data in all of these environments,^{2–4} when using frequency modulation (FM) AFM.⁵ This article extends the discussion to low- Q environments (near and below Q values of 1), where amplitude modulation (AM) AFM is the preferred dAFM method.

Section II discusses problems with piezoacoustic excitation that are unique to low- Q environments – in contrast to the well-behaved photothermal excitation.⁶ Afterwards, the design of our photothermal excitation unit – dubbed “the photothermal panther” – is presented and its performance is benchmarked in water. Then, photothermal excitation is employed for imaging and force spectroscopy on Au(111) in 1-butyl-3-methylimidazolium hexafluorophosphate [BMIM][PF₆] – a highly viscous ionic liquid. The photothermal dAFM measurement is compared to simultaneously acquired static AFM (sAFM) data, as both provide independent measurements of the solvation stiffness profile. Finally, limitations and complications that pertain to dAFM in low- Q environments are discussed.

II. PROBLEMS WITH PIEZOACOUSTIC EXCITATION

The benefits of photothermal excitation over piezoacoustic excitation in FM-AFM have recently been outlined in great detail.⁴ The “forest of peaks”⁷ observed using piezoacoustic excitation severely complicates the interpretation of the measured signals. In fact, accurate recovery of the conservative and dissipative forces may become impossible if the temperature of the instrument changes by as little as a few mK because the “forest of peaks” is temperature-dependent⁴ – it can drift and distort throughout the experiment.

Driving the cantilever at a fixed frequency greatly simplifies the interpretation of data as the frequency-dependence of the piezoacoustic excitation can be disregarded. This fact favors the use of AM-AFM for piezoacoustic excitation in liquids. However, the ratio of the cantilever excitation that arises from fluid vibrations (fluid-borne excitation), as opposed to movement of the cantilever base (structure-borne excitation),⁸ is unknown *a priori*; knowledge of this ratio is necessary for extracting quantitative force and dissipation measurements.⁹

Nevertheless, fundamental problems with piezoacoustic excitation persist in low- Q environments when used in conjunction with the optical beam deflection method:¹⁰ the measured oscillation amplitude of the cantilever and the true oscillation of the tip do not relate in any simple manner, as is graphically represented in Figure 1.

To illustrate this problem, we have used recent modelling of cantilever dynamics in liquids⁹ to plot the transfer function of the cantilever in the limiting case of structure-borne

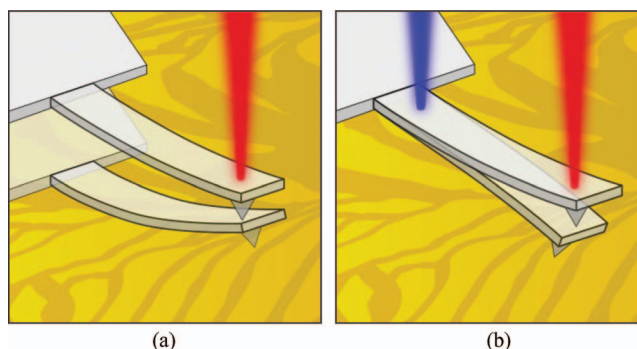


FIG. 1. (a) Piezoacoustic excitation drives the cantilever by moving the base of the cantilever, leading to complex cantilever dynamics that are frequency dependent: the measured angle of the cantilever tip does not relate to oscillation amplitude in any simple way for Q factors around and below 1. (b) Photothermal excitation drives the cantilever via stress-induced cantilever bending: the shape of the cantilever is well defined. (Artistic rendition of cantilevers and gold background courtesy of Magdalena Wielopolski).

loading only. We restrict the following discussion to the first eigenmode, as it suffices to illustrate the primary problem at hand. Figure 2 demonstrates that the *measured* oscillation amplitude strongly deviates from the *true* amplitude if it is driven off-resonance. In other words, the deflection sensitivity (in units of nm/V) is only valid around the resonance. Conversely, photothermal excitation has a constant sensitivity throughout the usable spectrum because the bending shape is frequency-independent.¹¹ Figure 2(b) suggests that a measurement of oscillation amplitude is reliable throughout the spectrum when using photothermal excitation, as opposed to piezoacoustic excitation.

This calibration predicament becomes especially problematic in overdamped environments ($Q < 0.5$), where the cantilever is excited below resonance. In fact, it would perhaps be foolish to excite the cantilever at its natural frequency, because the second eigenmode may have a larger response at that frequency. In any case, for piezoacoustic excitation, the dAFM sensitivity becomes a function of the drive frequency, the natural frequency, the Q factor, and the ratio of fluid-borne to structure-borne excitation. Calibrating the AFM sensitivity becomes difficult, if not impossible.

The above-mentioned problems do not only affect interpretation of acquired data, they can also prevent regular topographical imaging. Depending on the ratio between fluid-borne and structure-borne excitation, the measured amplitude may increase or decrease as the tip approaches the surface, potentially prohibiting stable feedback required for imaging. For example, if structure-borne excitation dominates, the base of the cantilever moves with an amplitude larger than the cantilever tip, as illustrated in Figure 1(a). In that case, the measured angular deflection of the cantilever becomes *larger*

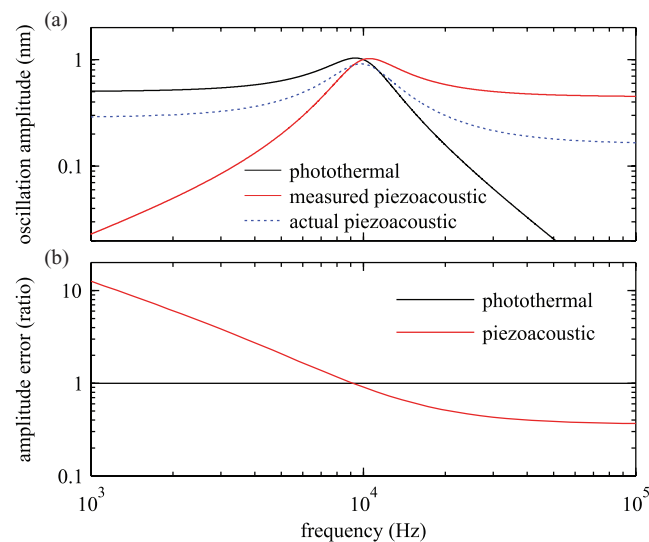


FIG. 2. (a) The first eigenmode of a driven cantilever with $Q = 2$ is simulated for photothermal excitation (with fixed force amplitude) and for piezoacoustic excitation (with fixed base amplitude) around the natural frequency (10 kHz). The photothermal response is simply that of a harmonic oscillator, i.e., the transfer function of the cantilever. As illustrated in Figure 1(b), the amplitude measured by piezoacoustic excitation does not correspond to the actual oscillation amplitude, except near the resonance frequency. (b) In other words, there is an amplitude calibration error when driving the cantilever off-resonance, which becomes inevitable for very low Q environments.

as the cantilever approaches the surface, rendering AM-AFM imaging difficult, if not impossible.

All the above-mentioned problems are resolved by employing photothermal excitation instead of piezoacoustic excitation.

III. THE PHOTOTHERMAL PANTHER

The photothermal panther is a retrofit to our existing home-built electrochemical (EC) AFM¹² designed for atomic-scale friction force microscopy in electrochemical environments.¹³ The only hardware modification to the previous design was the addition of a magnetic docking stage that allows the panther to be mounted effortlessly and rigidly with $\sim \mu\text{m}$ repeatability.

A. Optomechanical design

The design of the photothermal panther and its integration to the existing ECAFM is best explained graphically. This section describes some additional details, with reference to Figure 3.

A 20 mW blue laser-diode (DL-LS5042, Sanyo) light beam is collimated to ~ 1 mm by an aspheric collimation lens (352610-A, Thorlabs) with 4 mm effective focal length. The collimated light beam is reflected off a polarizing beamsplitter towards a 567 nm longpass dichroic mirror (DMLP567R, Thorlabs) that combines the red detection light beam and the blue excitation light beam. The existing optics of the ECAFM focus both light beams onto the cantilever, as well as rotate their polarization directions by 90° . The rotation in polarization guides the red light towards the photodetector after reflection, as well as prevents blue light from returning into the blue laser-diode which could cause lasing instabilities. Instead, the blue light is mostly absorbed by a yellow filter, which also acts as a sight glass for aiding the alignment of both light beams onto the cantilever. Two micrometer thumbscrews control the rotation angle of the laser-diode and the beamsplitter, thereby enabling 2-axis positioning of the blue laser onto the cantilever.

Additionally, since the previous description of our home-built ECAFM,¹² the collimated diameter of the detection light beam was reduced to 0.65 mm, and the effective focal length was increased to 25 mm. These changes reduced the divergence of the light beam by $4.5\times$, and therefore reduced the detection noise by the same ratio.¹⁴

The fully assembled ECAFM 3D technical drawing and the internal components can be interactively viewed in Figure 4.

B. Electronics

The blue laser-diode is driven in constant-power mode (WLD3343, Wavelength Technology) by using the integrated photodetector of the laser-diode for feedback. The drive current is modulated at 300 MHz using a voltage-controlled oscillator (POS-535+, Mini-Circuits) to

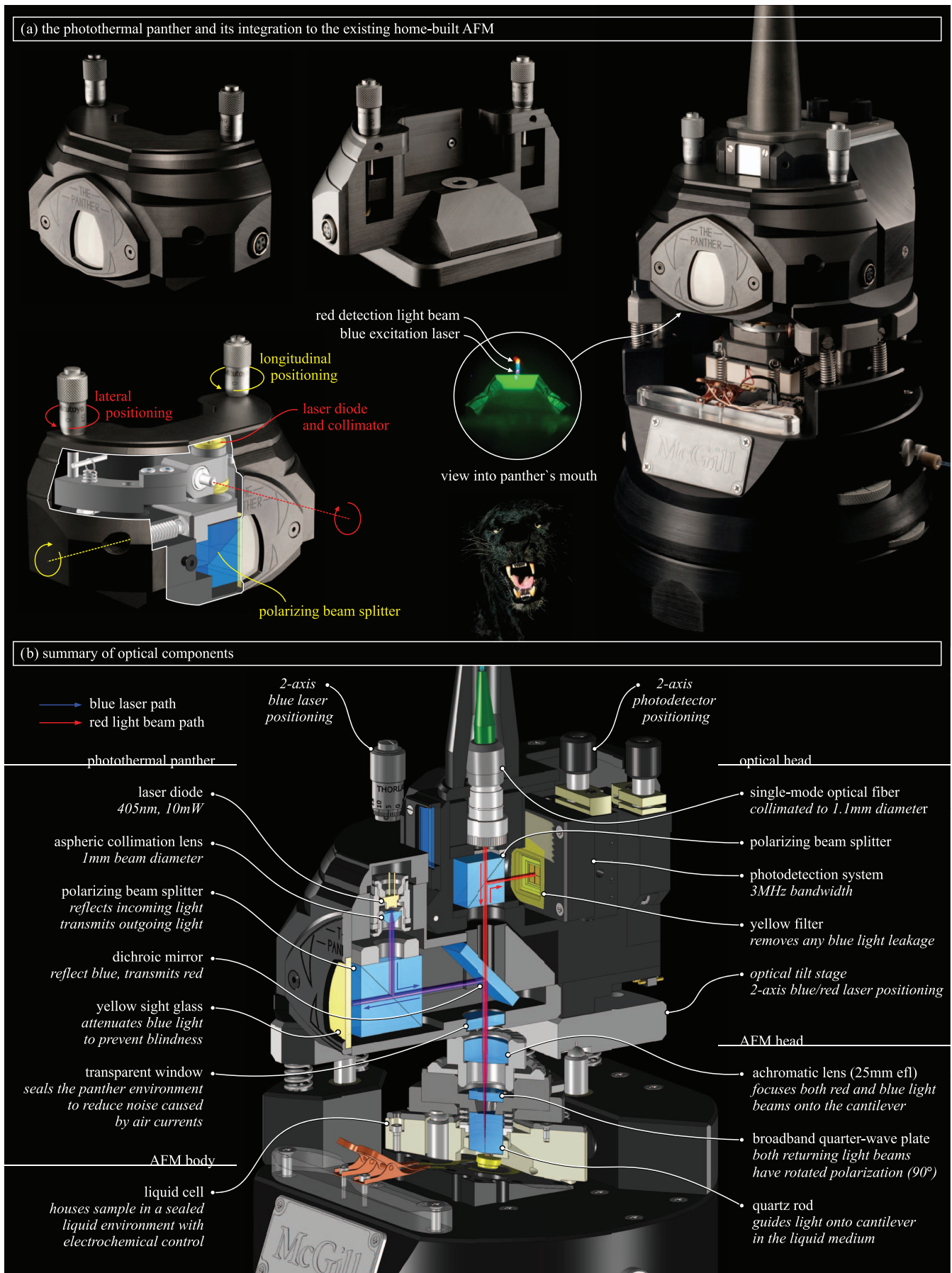


FIG. 3. The photothermal panther integrates a blue light beam into the existing AFM optical system to enable photothermal excitation of the cantilever.

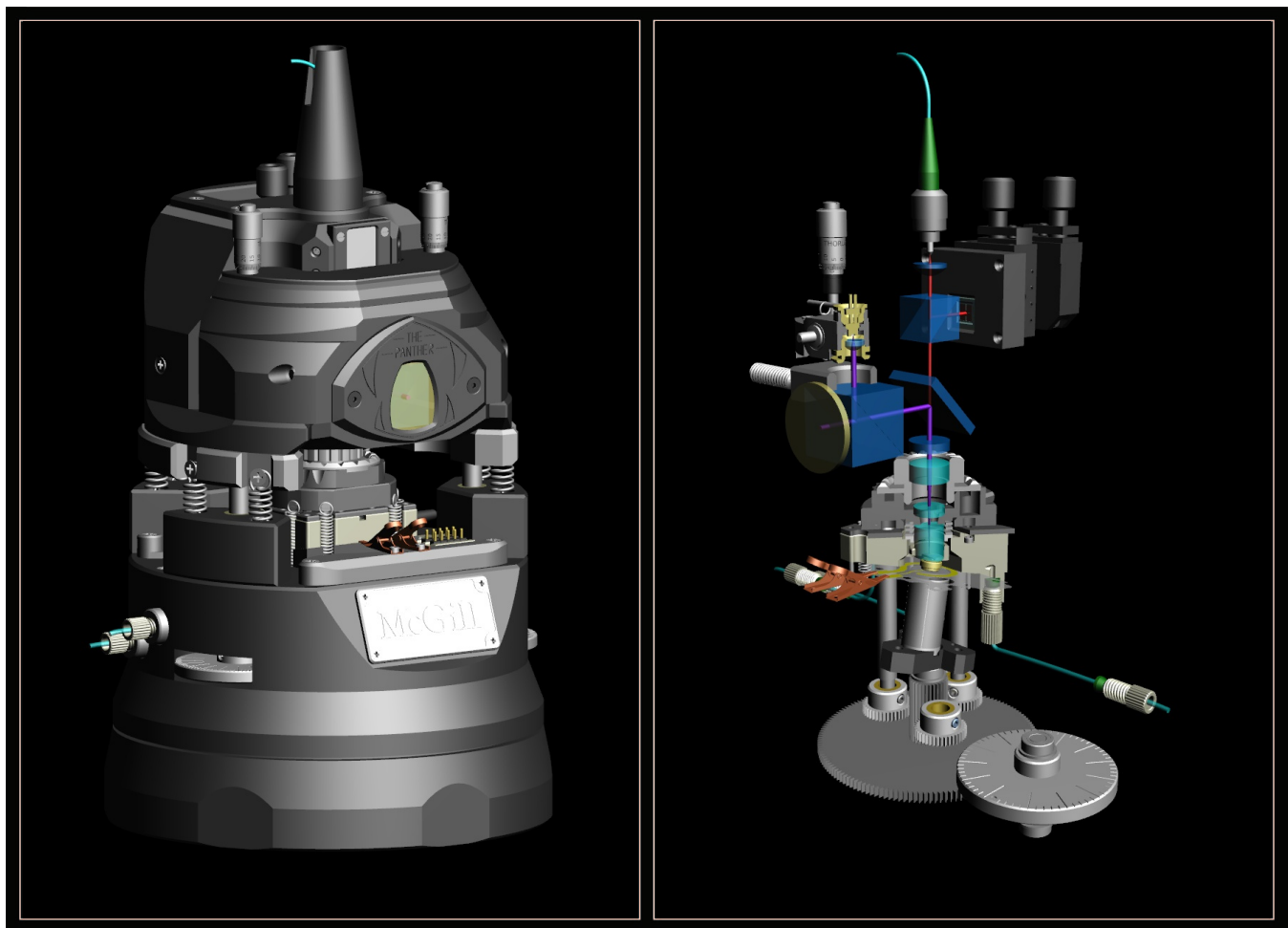


FIG. 4. Interactive 3D technical drawings of (a) the assembled ECAFM and (b) the internal optics and mechanics. Click image to activate. Use ctrl, shift, to zoom and pan.

reduce optical feedback and interference as described in Ref. 15.

Most importantly, the blue light power is modulated for photothermal excitation of the cantilever using a power splitter/combiner (PRSC-2050, Mini-Circuits). An input AC drive signal modulates the laser power output with a modulation depth determined by the drive amplitude. The circuit allows modulation of the laser power for frequencies between 1 kHz and 3 MHz, which covers the range of typical cantilever drive frequencies.

Also, our previous controller was replaced by the Nanonis SPM controller, allowing reliable imaging, the acquisition of transfer functions, and enabling fast force spectroscopy.

IV. PROOF-OF-PRINCIPLE IN MODERATE Q

We first demonstrate the capabilities of the photothermal panther in a moderate Q environment – water – where a clear cantilever resonance peak is observable. A gold-coated cantilever was used because it has higher photothermal efficiency than an uncoated one.¹⁶

A photothermally driven transfer function of the cantilever is shown in Figure 5(a). Overlaid is a fit to a harmonic oscillator model with a multiplicative $1/f$ background;

the model fits the data impeccably. The $1/f$ background (with an exponent of 0.36 set as a free fitting parameter) is attributed to the frequency-dependence of the photothermal driving efficiency, i.e., the photothermal excitation transfer function.⁴

The close agreement to the harmonic oscillator model is reassuring, as any AM-AFM theory^{1,17,18} used to interpret the magnitude and phase response throughout the experiment is based on the assumption that the cantilever can be described as a harmonic oscillator.

In Figure 5(b), the linearity of the system is demonstrated by driving the cantilever on-resonance at high power (15 mW at roughly 50% modulation depth) and measuring its deflection. A sinusoidal fit suggests highly linear behaviour; the residual plot deviates by no more than 0.3% of the oscillation amplitude (not shown).

Finally, the imaging capability of the system is illustrated in Figure 5(c) by the constant-amplitude topography image of Au(111) steps acquired in water using AM-AFM.

V. IMAGING IN OVERDAMPED ENVIRONMENTS

A gold sample was imaged in [BMIM][PF₆] using AM-AFM. Figure 6 presents a constant-amplitude topography image of a Au(111)-oriented grain, along with the phase signal

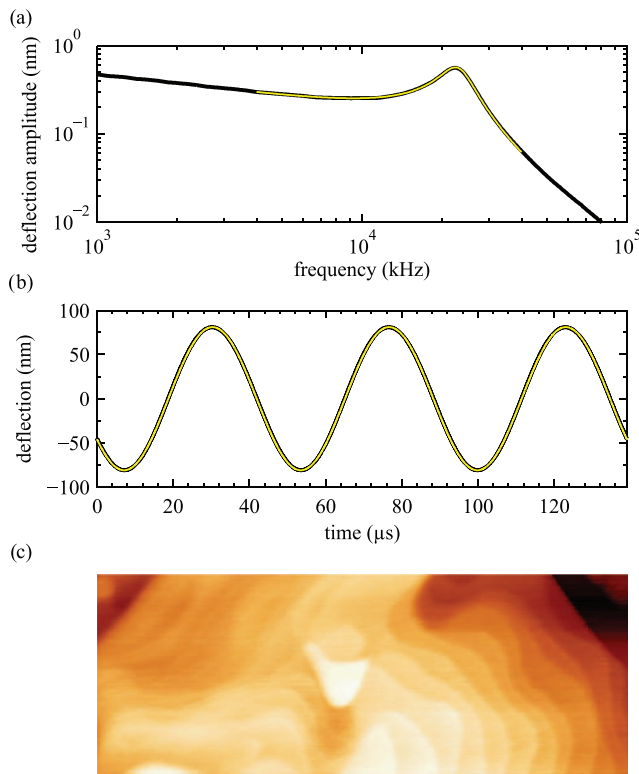


FIG. 5. (a) The photothermally driven cantilever amplitude response in water far from the surface. Cantilever stiffness: 1.34 N/m and Q : 3.6. A harmonic oscillator function with $1/f$ background is fit and overlaid. (b) Driving the cantilever on-resonance with a 8 mW modulation amplitude demonstrates the linearity of the system up to large oscillation amplitudes. A sinusoidal function was fit and overlaid. (c) Constant-amplitude topography image of Au(111) in water using photothermal AM-AFM. (Scan width: 500 nm; scan speed: 3 lines/s; pixel acquisition rate: 1 kHz).

and amplitude error signal. The subtle variations in topography loosely correlate with the unidentified objects clearly seen in the phase image. It was impossible to image the underlying Au(111) steps using dAFM, despite the high cantilever stiffness (28.5 N/m). In fact, this cantilever was too soft to penetrate the last layer of ionic liquid, necessary to observe the gold surface. The root of this problem will be discussed more thoroughly in Sec. VII.

Due to the low stiffness of the cantilever, it was necessary to switch imaging methods to sAFM in order to penetrate last layer and reveal the underlying Au(111) steps, as shown in Figure 6. Interestingly, there is a fine line between imaging and damaging the underlying gold substrate: a 40 nN set point was necessary to image, while 150 nN caused significant damage to the Au(111) surface, as observed by the damaged square area in the sAFM image in Figure 6.

Interestingly, switching between dAFM and sAFM with a single cantilever extends the dynamic range of usable force set points, allowing the imaging of both the solid surface and its solvation layers.

VI. FORCE SPECTROSCOPY IN OVERDAMPED ENVIRONMENTS

After imaging the surface, force spectroscopy was performed in the center of the Au(111) grain seen in Figure 6.

A. Calibration

The dynamic cantilever stiffness had been determined prior to imaging from a power spectral density (PSD) in air, using the Sader method^{19,20}: $k_c = 28.5$ N/m. Immediately before the force spectroscopy experiment, the deflection sensitivity of the AFM was calibrated $\sim 1 \mu\text{m}$ from the surface by measuring a PSD of the cantilever deflection in the ionic liquid, as seen in Figure 7.

A PSD was measured with the blue laser-diode both turned on and off, in order to verify that the blue light was not affecting the cantilever deflection signal in the frequency range of interest.²¹ The blue light causes additional $1/f$ cantilever bending below 2 kHz because of the coupling to light power fluctuations caused by the gold coating.²²

These verifications confirm that the measured PSD is in fact a thermal spectrum of the cantilever above 2 kHz. Because the cantilever is overdamped, its first eigenmode can be modelled as a massless harmonic oscillator, using the formalism proposed in a recent communication.²³ In this case, the cantilever spectrum is accurately modelled as a first-order low-pass filter driven by a white thermal force spectrum that

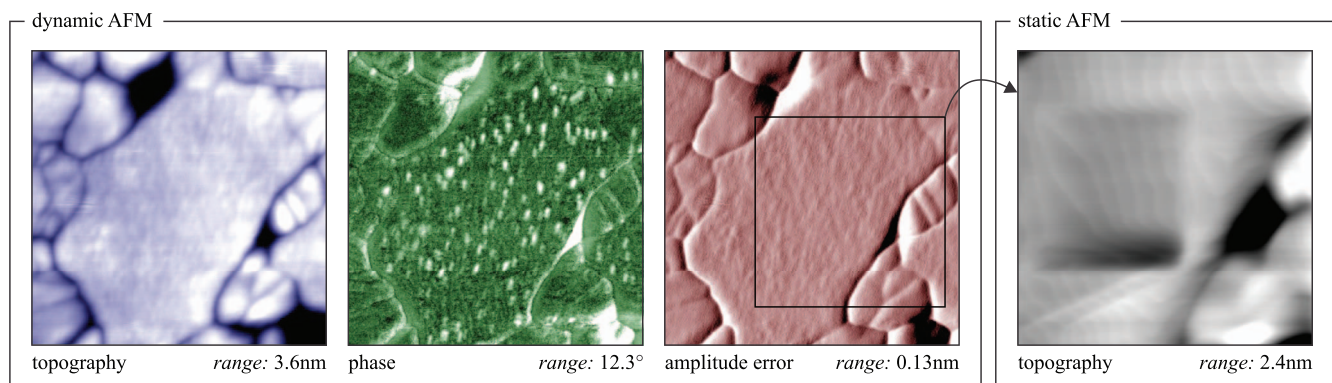


FIG. 6. Dynamic (AM) AFM was used to image Au(111) in [BMIM][PF₆]. Gold steps could not be observed as the range of imaging setpoints only allows the imaging of solvation layer above the surface. Switching to static AFM enables the imaging of underlying Au(111) with a 40 nN setpoint; however, a 150 nN setpoint damages the surface which can be observed as a square in the image from the previous scan. (Image size: 300 nm \times 300 nm; scan speed: 5 lines/s; pixel acquisition rate: 5 kHz).

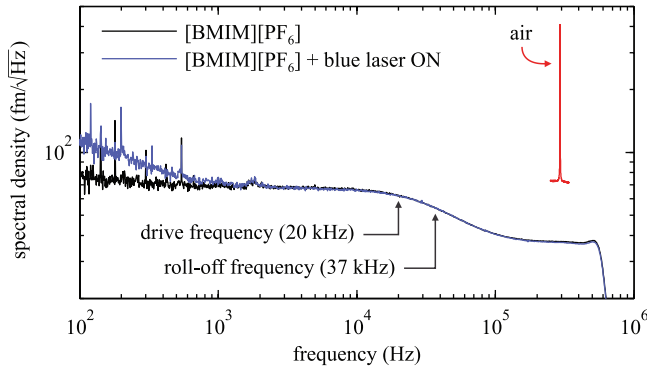


FIG. 7. Thermal spectrum of the cantilever in air, used to calibrate the stiffness, and the thermal spectrum in [BMIM][PF₆] near the gold surface, used to calibrate the damping. Turning on the blue light confirms that the measured spectrum around 10 kHz is in fact a thermal spectrum, which therefore can be used to calibrate the AFM using the fluctuation-dissipation theorem and the measured damping.

can be determined by the fluctuation-dissipation theorem.²⁴ In summary, the thermal PSD for overdamped cantilevers equals

$$\frac{4k_B T}{k_c(2\pi f_{ro})} \frac{1}{1 + (f/f_{ro})^2}, \quad (1)$$

where f_{ro} is the roll-off frequency of the low-pass filter, and $k_B T$ is the thermal energy of the harmonic oscillator. Fitting the measured PSD in Figure 7 with this equation determines f_{ro} and calibrates the sensitivity of the AFM.

Finally, the transfer function of the cantilever can be defined at any drive frequency f by its magnitude

$$|C| = \frac{1}{k_c} \frac{1}{\sqrt{1 + \left(\frac{f}{f_{ro}}\right)^2}} \quad (2)$$

and phase

$$\theta_C = -\text{atan}\left(\frac{f}{f_{ro}}\right). \quad (3)$$

B. Results

Two hundred approach curves were performed in the span of 100 s. Both dAFM and sAFM signals were measured simultaneously. The dAFM was performed by oscillating the cantilever with a constant photothermal driving force of 7 nN amplitude at 20 kHz, and measuring its magnitude response $|C|$ and phase response θ_C . All 200 approach curves were highly reproducible, as demonstrated by the movie in Figure 8. The high level of reproducibility (within noise) suggests that the tip remained stable throughout the measurement and warrants averaging the 200 approach curves.

Figure 9(a) presents the averaged dAFM data, along with the averaged sAFM deflection. Note that the dAFM oscillation amplitude was below 200 pm, which is much smaller than the [BMIM][PF₆] ion-pair diameter, and the sAFM deflection remained below 60 pm across the solvation profile. Therefore, the dAFM and sAFM are independent measurements²⁵ of the solvation profile.

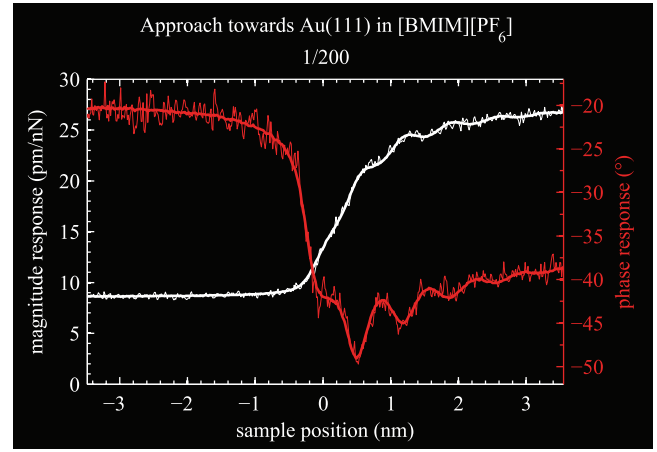


FIG. 8. Movie of 200 approach curves towards Au(111) in [BMIM][PF₆], acquired after the calibration in Figure 7. The magnitude response $|C|$ and phase response θ_C of the cantilever is shown. The thick lines represent the averaged profiles, while the thin lines represent single approach curves. Two approach curves were acquired per second, with an approach speed of 70 nm/s. The sample position was corrected for drift; the drift was mostly linear with a rate of 2 pm/s. No isolation hood was used. (enhanced online) [URL: <http://dx.doi.org/10.1063/1.4712286.1>].

In Figure 9(b), the interaction stiffness and damping measured by dAFM were obtained by²³

$$\gamma_i = -\frac{1}{\omega} \left[\frac{\sin \theta_C}{|C|} - \frac{\sin \theta_{C_s}}{|C_s|} \right] \quad (4)$$

and

$$k_i = \frac{\cos \theta_C}{|C|} - \frac{\cos \theta_{C_s}}{|C_s|}, \quad (5)$$

where $|C_s|$ and θ_{C_s} are the magnitude and phase response measured at the start of the experiment during the calibration procedure. Although the calibration of the cantilever assumed a massless harmonic oscillator model, Eqs. (4) and (5) apply for AM-AFM at all Q values, and are mathematically identical to standard AM-AFM theory.¹⁸

The interaction force measured by sAFM is proportional to the tip position, related by k_c , and the corresponding stiffness, plotted in Figure 9(c), is calculated as the derivative of interaction force with respect to tip-sample distance.

VII. DISCUSSION

Despite resolving all the complications that arise due to piezoacoustic excitation (discussed in Sec. II) by the use of clean photothermal excitation, the interpretation of measured signals remains non-trivial. This section discusses the results in Figure 9.

A. Offset in stiffness and damping

Note that there are offsets in stiffness and damping at 4.5 nm tip-sample distance for the dAFM data in Figure 9(b). These offsets represent changes in stiffness and damping between the 4.5 nm and $\sim 1 \mu\text{m}$ tip-sample distances; the latter is the distance at which the cantilever was calibrated.

The offset in damping can be mostly attributed to squeeze film damping of the cantilever. The offset in stiffness is due

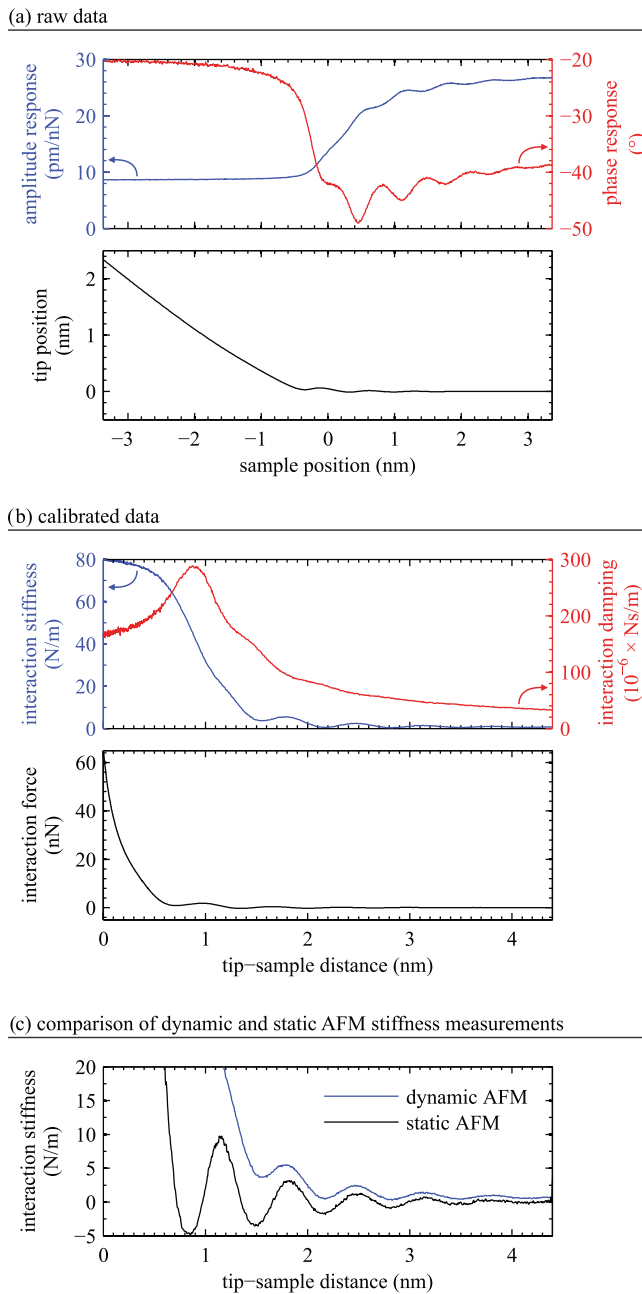


FIG. 9. (a) Averaged data from Figure 8 and the simultaneously acquired (averaged) deflection signal. (b) The measured data were converted into physical signals. (c) The independent measurements of stiffness (dynamic and static) are plotted together. The two correspond very well (up to an offset) far from the surface, however dynamic AFM breaks down near the surface because the interaction stiffness becomes a large fraction of the cantilever stiffness (28.5 N/m).

to either a calibration error or a true change in effective cantilever stiffness. These offsets are instrumental artifacts that should be disregarded during the interpretation of tip-sample physics, and could be minimized by calibrating the cantilever much closer to the sample surface, say 15 nm instead of 1 μ m away. In other words, these offsets relate to cantilever-sample interactions, rather than tip-sample interactions.

Nevertheless, the offset in stiffness is worrisome, as it suggests that the assumption of a constant cantilever stiffness (in air versus liquid) may be wrong. In fact, because the

damping and mass loading of the cantilever are not uniform across the full length of the cantilever (due to the proximity to the surface at an angle), the modal shape of the cantilever may be skewed and cause a change in effective stiffness²⁶ that depends on the cantilever-sample distance. For the data in Figure 9, this effect is small.

B. Dynamic vs static stiffness

Figure 9(c) overlays the stiffness profile as measured by the dynamic and static AFM methods. Disregarding the offset in dynamic stiffness, explained in Sec. VII A, the two datasets agree very well beyond 2 nm from the surface. But below 2 nm, for the two or three last hydration layers, both methods deviate significantly.

Hooke's law, used to interpret the sAFM measurement, remains accurate even for situations where the interaction stiffness greatly exceeds the cantilever stiffness – as long as the quasistatic condition is respected and no jump instabilities occur. We believe the sAFM stiffness profile in Figure 9(c) to be very accurate.

On the other hand, the stiffness profile extracted from dynamic AFM becomes questionable close to the surface because the solvation layer stiffness rises to a significant percentage of the cantilever stiffness (>10%). Therefore, the point-mass model approximation (Eq. (1)) begins to break down in proximity to the sample surface as the shape of the pinned cantilever takes precedence.²⁷ Stiffer cantilevers are required to obtain accurate data for the solvation layers closest to the surface. Note that this shortcoming is universal to all dAFM techniques, irrespective of the Q factor of the cantilever, and therefore does not affect the validity of the massless model used to calibrate the cantilever. Even if the calibration (Eqs. (1)-(3)) is perfectly accurate, the assumption of a point-mass that led to the derivation of AM-AFM theory (Eqs. (4) and (5)) is violated, and the dynamic stiffness measurement is expected to be incorrect.

C. Oscillations in damping

Damping could not be measured with sAFM as it is an intrinsically velocity-dependent quantity. It is however expected that the damping profile measured by dAFM loses accuracy in proximity to the surface for the same reasons as the stiffness profile, described in Sec. VII B.

The monotonically increasing damping profile as the tip approaches to 2 nm from the surface can therefore be trusted. However, the oscillations in damping between 1–2 nm are highly questionable, and the decrease in damping below 1 nm is definitely meaningless.

D. Tip-sample distance

A commonly arising issue when imaging in liquids is the determination of the tip-sample distance. The plot thickens in viscous ionic liquids at the gold electrode as the last liquid layer may require very large pressure to be displaced by the tip. Therefore, there is no clear force regime between the liquid removal, and the compression and damage of the gold

electrode; i.e., there is no hard-contact regime which can be used to zero the tip-sample distance. In fact, it is possible that the gold surface and the tip undergo significant deformation before the last liquid layer is displaced. This observation is consistent with the low damage threshold (somewhere between 40 nN and 150 nN) of the gold sample observed in Figure 6. Given these complications, the tip-sample distance in Figure 9 is poorly defined and somewhat arbitrary.

VIII. CONCLUSIONS

Our home-built AFM¹² was retrofit with a photothermal excitation unit with minimal modification to the original design. Photothermal excitation provides a reliable method for exciting cantilevers in liquid environments and allows much easier interpretation of tip-sample physics than in the case of piezoacoustic excitation.

Static and dynamic AFM can serve as complimentary techniques for imaging the solid-liquid interface, allowing imaging of both the solid surface and liquid layers, respectively. In essence, both imaging methods can be combined to span a higher dynamic range of force measurements and imaging setpoints.

A comparison between dynamic and static force spectroscopy performed simultaneously suggests that dynamic AFM reliability decreases as the interaction stiffness increases up to and above the cantilever stiffness. This is explained by the fact that the cantilever changes modal shape to a pinned cantilever, making the original point-mass approximation fail. Cantilevers much stiffer than the interaction should be used to maintain accurate recovery of stiffness and damping profiles.

The complications that arise when imaging in viscous liquids are plentiful; they relate to cantilever dynamics and strong tip-sample interactions (relative to the cantilever stiffness). Photothermal excitation allowed us to identify and address these difficulties confidently, because all the instrumental complications caused by piezoacoustic excitation were abolished.

ACKNOWLEDGMENTS

We acknowledge valuable discussions with Hirofumi Yamada, Daniel Kiracofe, and William Paul, as well as the

generosity of SPECS Surface Nano Analysis Inc., NSERC, FQRNT, and Cifar.

- ¹R. García and R. Perez, *Surf. Sci. Rep.* **47**, 197–301 (2002).
- ²R. Proksch and S. V. Kalinin, *Nanotechnology* **21**, 455705 (2010).
- ³A. Labuda, Y. Miyahara, L. Cockins, and P. Grütter, *Phys. Rev. B* **84**, 125433 (2011).
- ⁴A. Labuda, K. Kobayashi, D. Kiracofe, K. Suzuki, P. H. Grütter, and H. Yamada, *AIP Adv.* **1**, 022136 (2011).
- ⁵T. R. Albrecht, P. Grutter, D. Horne, and D. Rugar, *J. Appl. Phys.* **69**, 668–673 (1991).
- ⁶G. C. Ratcliff, D. A. Erie, and R. Superfine, *Appl. Phys. Lett.* **72**, 1911 (1998).
- ⁷T. E. Schäffer, J. P. Cleveland, F. Ohnesorge, D. a. Walters, and P. K. Hansma, *J. Appl. Phys.* **80**, 3622 (1996).
- ⁸X. Xu and A. Raman, *J. Appl. Phys.* **102**, 034303 (2007).
- ⁹D. Kiracofe and A. Raman, *Nanotechnology* **22**, 485502 (2011).
- ¹⁰G. Meyer and N. M. Amer, *Appl. Phys. Lett.* **53**, 1045–1047 (1988).
- ¹¹To be exact, the bending shape converges to perfectly circular as $f \rightarrow 0$ because the cantilever temperature profile becomes uniform at long timescales. This suggests a frequency-dependence and a deviation from the first-eigenmode approximation used in this article. However, the deviations are small (a few percent) in the usable frequency range for dAFM using photothermal excitation, and are negligible in our comparison with piezoacoustic excitation where deviations can exceed an order of magnitude.
- ¹²A. Labuda, W. Paul, B. Pietrobon, R. B. Lennox, P. H. Grütter, and R. Bennewitz, *Rev. Sci. Instrum.* **81**, 083701 (2010).
- ¹³A. Labuda, F. Hausen, N. N. Gosvami, P. H. Grütter, R. B. Lennox, and R. Bennewitz, *Langmuir* **27**, 2561–2566 (2011).
- ¹⁴A. Labuda and P. H. Grütter, *Rev. Sci. Instrum.* **82**, 013704 (2011).
- ¹⁵T. Fukuma, M. Kimura, K. Kobayashi, K. Matsushige, and H. Yamada, *Rev. Sci. Instrum.* **76**, 053704 (2005).
- ¹⁶D. Kiracofe, K. Kobayashi, A. Labuda, A. Raman, and H. Yamada, *Rev. Sci. Instrum.* **82**, 013702 (2011).
- ¹⁷S. N. Magonov, V. Elings, and M.-H. Whangbo, *Surf. Sci.* **375**, L385–L391 (1997).
- ¹⁸S. J. O’Shea and M. E. Welland, *Langmuir* **14**, 4186–4197 (1998).
- ¹⁹J. E. Sader, J. W. M. Chon, and P. Mulvaney, *Rev. Sci. Instrum.* **70**, 3967 (1999).
- ²⁰M. J. Higgins, R. Proksch, J. E. Sader, M. Polcik, S. Mc Endoo, J. P. Cleveland, and S. P. Jarvis, *Rev. Sci. Instrum.* **77**, 013701 (2006).
- ²¹O. Marti, A. Ruf, M. Hipp, H. Bielefeldt, J. Colchero, and J. Mlynek, *Ultramicroscopy* **42–44**, 345–350 (1992).
- ²²A. Labuda, J. R. Bates, and P. H. Grütter, *Nanotechnology* **23**, 025503 (2012).
- ²³A. Labuda and P. Grütter, *Langmuir* **28**, 5319–5322 (2012).
- ²⁴M. T. Clark, J. E. Sader, J. P. Cleveland, and M. R. Paul, *Phys. Rev. E* **81**, 046306 (2010).
- ²⁵S. Kawai, T. Glatzel, S. Koch, B. Such, A. Baratoff, and E. Meyer, *Phys. Rev. B* **80**, 085422 (2009).
- ²⁶D. Kiracofe and A. Raman, *J. Appl. Phys.* **107**, 033506 (2010).
- ²⁷U. Rabe, K. Janser, and W. Arnold, *Rev. Sci. Instrum.* **67**, 3281 (1996).